NINETEENTH EUROPEAN ROTORCRAFT FORUM

Paper n° G13

FLAP, LEAD-LAG AND TORSION STABILITY OF STOP-ROTORS

by

U. ARNOLD, G. REICHERT

TECHNICAL UNIVERSITY OF BRAUNSCHWEIG, GERMANY

September 14-16, 1993
CERNOBBIO (Como)
ITALY

ASSOCIAZIONE INDUSTRIE AEROSPAZIALI
ASSOCIAZIONE ITALIANA DI AERONAUTICA ED ASTRONAUTICA

Abstract

Horizontally stoppable rotors are susceptible to certain instabilities, particularly at high advance ratios. This paper presents a straightforward analytical model that considers the specific operating conditions as strong parametric excitation (due to periodic coefficients), reverse flow and low rotor speed. Different mathematical methods have been applied to determine the forced solution and the stability. Most calculations have been performed based on numerical integration and FLOQUET theory. Deriving the FLOQUET transition matrix from the perturbed nonlinear equations proved to be quite efficient. This allows the easy inclusion of the important influence of the periodic trim solution.

First, the behavior of the isolated degrees of freedom is discussed. The lead-lag motion was found to be quite insensitive to parametric excitation, even at very high advance ratios. The flapping and torsional motion, however, are strongly affected by parametric effects. The results show the typical structure of STRUTT's stability diagram. Then, the modification of the stability boundaries due to coupling effects is described. Flap-torsion interaction degrades the stability of stop-rotor blades. In the last part, some ideas and results are presented which show how to augment the flap stability and how to reduce the flap amplitudes by active control.

Notation

c_β , c_ζ , c_Θ	equivalent hinge spring stiffness
m	blade mass
$r = xR$	blade radius coordinate
t	time
$T = 2\pi/\Omega$	time of one rotor revolution;
T	rotor thrust
v_t , v_n	tangential / normal velocity at the blade section
V	rotorcraft forward speed
y_{cg} , y_{ac}	location of blade section center of gravity (c.g.) / normal flow aerodynamic center (a.c.$_1$) behind the feathering axis (f.a.)
α	blade section angle of attack
β	flap angle
γ	LOCK number / 2
$\delta = w_i/(\Omega R)$	inflow ratio
ζ	lag angle
$\vartheta = \vartheta_{con} + \vartheta_1 x + \Theta$	feathering angle, composed of pitch, twist & torsion angle
λ/Ω	eigenvalue of the corresponding system with constant coefficients
$\mu = V/(\Omega R)$	advance ratio
$\psi = \Omega t$	blade azimuth angle
$\overline{\omega}^{nr} = \frac{\sqrt{c/J}}{\Omega_{nom}}$	nonrotating natural frequency nondimensionalized by the nominal rotor speed
$\overline{\Omega} = \Omega/\Omega_{nom}$	nondimensional rotor speed
$(\,)' = \partial(\,)/\partial\psi$	derivative with respect to ψ
$\dot{(\,)} = \partial(\,)/\partial t$	derivative with resp.to the time

Further definitions and quantities can be found in Table 1, Figure 2 or in the appendix.

Introduction

Aircraft which combine the take-off and landing performance of a helicopter with the forward speed capability of a fixed wing aircraft have been studied for almost three decades. Beside the tilt-rotor, which seems to have become the most successful variant, several other concepts have been proposed since then. One of them is the stop-rotor composite aircraft, as described in Refs.[1], [10], [13], [16] and [17]. Although some theoretical and experimental work has been done, none of those projects has reached the prototype stage.

The concept is to completely convert the rotorcraft into a fixed-wing aircraft by stopping, folding and stowing the rotor(s). First, the vehicle accelerates to the transition speed in helicopter mode. Then, all of the lift is shifted from the rotor(s) to the wing, and the necessary propulsive force is generated by switching a convertible engine from shaft-power mode to fan-jet mode. Finally, the unloaded rotor(s) can be stopped horizontally. The stopped blades may be folded and stowed or, as other concepts propose, be used as fixed wings.

While many fundamental investigations have been conducted concerning the stability of helicopter blades, few publications discuss the behavior beyond the typical helicopter flight envelope at very high advance ratios, see Refs.[12], [15], [17] and [19]. This paper presents some basic results that have been obtained from relatively simple blade models. The primary aim is to show the structure of possible instabilities, the important influence of the forced (i.e. trim) solution, and some details of rotor control.

The following table contains the data which has been used for all of the presented calculations. They are representative for a smaller 9.6 ton aircraft with two rotors side by side.

Rotor radius		R =	5 m
Blade chord		l =	0.3 m
blade mass per unit lenght		$\overline{m}$ =	7.5 kg/m
Aerodynamically effective blade range	from	A =	0.25
	to	B =	1.00
Lift curve slope		$C_{l\alpha}$ =	6.25
Profile drag coefficient		C_{d0} =	0.01
Equivalent hinge offset		a/R =	0.13
nominal rotor speed		Ω_{nom} =	50 rad/sec
air density		ρ =	1.225 kg/m³

Table 1: Reference data

High rotor acceleration and deceleration rates can suppress the occurrence of instabilities, as discussed in Ref.[2]. Nevertheless, this investigation is based on the assumption that stability and sufficiently small amplitudes should be assured at each steady rotor speed. This allows the safe interruption and reversal of the start/stop procedure in case of technical malfunction.

As will be shown later, the blade motion stability is dominated by parametric excitation. It therefore proved suitable to plot the eigenvalues versus the advance ratio. Of course, an equally important effect results from the reduction of the rotor speed. So it should be noted that the advance ratio in this paper is not used synonymous with the forward speed, but implicitly describes how the rotor angular velocity is decreased.

Modeling of Blade Motion

For this investigation, only one isolated blade has been considered, and all interactions with other blades, the wing or the fuselage have been neglected. The considered flapping, lagging and torsional blade motions are described by rotations of the rigid blade about fictitious hinges, see Fig.1. The equivalent hinge offsets and spring stiffnesses have been adjusted to approximate the first eigenfrequencies and eigenmodes of a corresponding hingeless rotor blade.

For the presented calculations, the rotor has been assumed to be completely unloaded. Furthermore, the rotor disk plane has no incidence with respect to the free-stream velocity. These assumptions correspond to the optimal operating condition for the start/stop procedure. Therefore, any stop-rotor vehicle should be able to meet this trim condition during the conversion (e.g. by using conventional control surfaces).

Flapping Motion

The aerodynamic forces acting on the blade are derived from linear two-dimensional quasi-steady strip theory. This leads to the local flapping moment

$$\mathrm{d}M = \tfrac{\rho}{2} C_{l\alpha} l R^2 \left[\frac{v_n}{v_t} + \vartheta \right] v_t |v_t| (x - \tfrac{a}{R}) \mathrm{d}x$$

with the velocity components at the blade section

$$v_n = R\Omega \left[\delta - (x - \tfrac{a}{R})\beta' - (\mu \cos\psi)\beta \right]$$

$$v_t = R\Omega (x + \mu \sin\psi) \quad .$$

Reverse flow can be modeled by switching the sign of the lift coefficient in the corresponding blade section of the retreating blade. Periodic blade integrals $\overline{D}_n^R(\psi)$ (see Fig.3 and appendix) have been defined to retain the straightforward analytical formulation of the differential equations. Neglecting small quantities, we can write the linearized flapping equation of motion as

$$\beta'' + \gamma_\beta D_{11}(\psi)\beta' + \left[\gamma_\beta K_{11}(\psi) + K_{0_{11}}\right]\beta = \gamma_\beta\left[E_{11}(\psi)\vartheta_1 + E_{12}(\psi)\vartheta_{con} + E_{15}(\psi)\delta\right] + F_{0_1} ,$$

where the periodic coefficients $D(\psi)$, $K(\psi)$ and $E(\psi)$ describe the aerodynamic flap moments. The K_0 term represents the spring effect due to centrifugal and elastic forces, while F_0 describes the effect of the blade weight. All coefficients are listed in the appendix; for more details see Ref.[2].

Torsional Motion

For the normal working condition with flow from the leading edge, torsional moments can be kept sufficiently small by locating the feathering axis and the blade section center of gravity near the aerodynamic center at the 25% chord line. In the reverse flow region, however, the lift acts at approximately the 75% chord line and exhibits considerable torsional moments L, leading to a negative aerodynamic spring effect. Therefore, the torsional degree of freedom may be expected to have an important influence on the blade motion stability at high advance ratios (see Ref.[12]).

For this investigation, the blade model allows for arbitrary location of the center of gravity and the feathering axis, while the aerodynamic center is assumed to coincide with the 25% or 75% chord line respectively, see Fig.2. As for the flapping motion, these two different locations for normal and reversed flow can be considered by analytical expressions, consisting of both constant and periodic blade integrals $\overline{D}_n$ and $\overline{D}_n^R(\psi)$. To also include damping moments, the following approximation from the classical unsteady aerodynamic theory has been applied:

$$dL = -\tfrac{\rho}{8} C_{l\alpha} l^3 R(4\bar{y}^2|v_t| + \bar{y}v_t)\dot{\alpha}\,dx$$

$$L = -\tfrac{\rho}{8} C_{l\alpha} l^3 R^2\Omega\left[4\bar{y}\overline{D}_2^R + \bar{y}(\overline{D}_2 + \overline{D}_1\mu\sin\psi)\right]\dot{\alpha} .$$

The damping depends on the location of the feathering axis $\bar{y}$. Neglecting small terms, we can write the equation for the isolated torsional motion as

$$\Theta'' + \gamma_\Theta D_{22}(\psi)\Theta' + \left[\gamma_\Theta K_{22}(\psi) + K_{0_{22}}\right]\Theta = \left[\gamma_\Theta E_{21}(\psi) + E_{0_{21}}\right]\vartheta_1 + \left[\gamma_\Theta E_{22}(\psi) + E_{0_{22}}\right]\vartheta_{con} + \gamma_\Theta E_{23}(\psi)\vartheta'_{con} + E_{0_{24}}\vartheta''_{con} + \gamma_\Theta E_{25}(\psi)\delta + F_{0_2} .$$

The coupled flap/torsion equation can be found in the appendix.

Lead-Lag Motion

To analytically include reverse flow with the same formalism in the lead-lag motion as well, we must assume that the in-plane aerodynamic force due to the tilt of the local lift vector is small compared to the profile drag. Of course, this simplification is only applicable if the rotor is completely unloaded. Then, the aerodynamic in-plane moment becomes

$$dN = \tfrac{\rho}{2} C_{d0} l R^2 v_t|v_t|(x - \tfrac{e}{R})dx ,$$

where the square of the tangential flow component can be approximated by the linearized expression

$$v_t|v_t| = (R\Omega)^2\left[x + \mu\sin\psi - 2(x - \tfrac{e}{R})\zeta' - 2(\mu\cos\psi)\zeta\right]|x + \mu\sin\psi| .$$

This yields the following equation for the isolated lead-lag motion.

$$\zeta'' + \gamma_\zeta D_{33}(\psi)\zeta' + \left[\gamma_\zeta K_{33}(\psi) + K_{0_{33}}\right]\zeta = \gamma_\zeta F_3(\psi)$$

The coupled equation complete with all definitions is given again in the appendix, which also contains some nonlinear coupling terms that result from the coriolis forces. Beside these explicit equations, a numerical, nonlinear model has been used to study the influence of stall and compressibility. It is based on measured 360 deg. profile data and considers all nonlinear kinematic relationships as well.

Methods of Stability Calculation

As long as the differential equations can be kept linear, the classical Floquet theory is directly applicable to determine stability, as has been well documented in many publications.

The methods that have been used for the nonlinear equations in this investigation are summarized in Fig.4. The procedure consists of two parts: first, the determination of the interesting periodic forced solution and second, the investigation of that solution regarding stability.

Forced Solution

Since the periodic blade motions contain considerable higher-harmonic components at high advance ratios, harmonic balance (i.e. the approximation through an 1Ω expression) did not prove to be feasible. Figure 5 gives a typical example of the FOURIER transform of the flapping motion at $\mu = 1$ and $\mu = 10$. On the other hand, the numerical effort increases rapidly if one tries to balance the necessary number of harmonics.

A simple alternative is numerical stepwise integration. This is quite efficient as long as the blade motions are sufficiently damped. For weakly damped or even unstable solutions, a periodic shooting method must be used.

Stability of Forced Solution

The equations of motion are usually linearized about the known periodic solution by writing the corresponding perturbation equations about the equilibrium position. If the nonlinearities not allow for explicit derivation of the linear equations, numerical stepwise linearization can be performed.

A rarely applied method is based on determining the FLOQUET transition matrix directly from the nonlinear equations (compare Ref.[11]). The principle can be explained using Fig.6. The thin lines represent an equilibrium solution of the nonlinear periodic equation

$$\ddot{x} + 2D\Omega\dot{x} + (K_0 + K_c\cos\Omega t)\Omega^2 x^3 = u\Omega^2\cos(\Omega t + \varphi)\,,$$

which has to be determined in the first step. Then, for each column $\underline{\Phi}'_*$ of the transition matrix, the numerical integration is repeated with one of the state variables perturbed by a small parameter ε (thick lines). The deviations at the end of the integration interval correspond to the required matrix columns used to form the transition matrix $\underline{\underline{\Phi}}_* = \underline{\underline{\Phi}}(t_0 + nT)$. Since the periodic solution contains subharmonics of $\Omega/4$ in this example, the integration had to be performed over a time interval of $4T$. This procedure, here called the modified FLOQUET method, has been used successfully for some of the calculations presented below.

Figure 7 gives an impression of the numerical behavior of this method. The diagram shows the calculated damping of the flapping motion at $\mu = 5$ versus the magnitude of the perturbation parameter ε. The solid line refers to the trivial equilibrium solution, $\beta = \beta' = 0$, which one gets from the homogeneous equation with all forcing function terms canceled. The broken lines have been calculated for a forcing function that considers the effects of the blade weight and twist.

First, it is obvious that the periodic solution has in fact an important influence on the stability. Furthermore, the curves show that in this example ε should not exceed values of approximately $0.01\,\mathrm{rad}$ and $0.01^{\mathrm{rad}}/_{\mathrm{rad}}$; otherwise the nonlinearities deteriorate the stability results.

On the other hand, the perturbations must be considerably greater than the inaccuracies of the examined forced solution. The standard deviation between the discrete flap angles of the last two rotor revolutions has been used as an error criterion. As the example indicates, ε must be at least one order greater than this standard derivation. It is obvious that the periodic solution should be calculated only as accurate as necessary with respect to the computation time.

Evaluating the numerically integrated transient time history is a third method for calculating the stability of periodic solutions. However, quite sophisticated procedures must be applied to handle certain cases of parameter excitation.

Stability Results

The following results are presented in order to improve the understanding of the blade motion stability at very high advance ratios. Because of the applied simplifications, this work does not intend to investigate one concrete blade design in detail. Some results for the influence of fundamental blade parameters as LOCK number, hinge offset, artificial damping, etc. can be found in Ref.[2].

Isolated Flapping

Since the stop-rotor is unloaded when it operates at reduced rpm, many of the classical (coupled) blade instabilities will not occur. On the other hand, the strong parameter excitation at high advance ratios can drive even

the isolated flapping motion unstable. As can be seen in Fig.8, this flapping instability can easily be avoided by providing for a certain level of flap-hinge spring stiffness. With the data of Tab.1, a spring stiffness equivalent to a nonrotating natural frequency of $\bar{\omega}_\beta^{nr} = 0.1$ was found to be sufficient to assure stability. This low value is exceeded by most hingeless rotors.

The dotted lines show results from the linear equation, in which the periodic solution has no influence on the stability. The corresponding curves for the nonlinear equation (solid lines) describe the stability behavior of the equilibrium solution $\beta = \beta' = 0$. Since not all terms of the forcing function can be suppressed, this optimal condition is purely theoretical. Even the blade weight will cause a periodic response. However, the comparison shows that the linear model is reasonable in predicting the influence of reverse flow and compressibility. Likewise, the local stall effects at the boundary between the normal and reversed flow region proved to have only a minor effect on the calculated stability.

The stabilizing effect of a high nonrotating flapping frequency (i.e. a stiff equivalent flap spring) becomes more obvious in Fig.9. It shows the typical structure of STRUTT's stability diagram for the damped MATHIEU-TYPE equation.

Figure 10 illustrates what influence the trim solution can have on the flapping stability. With $\bar{\omega}_\beta^{nr} = 0.12$, the evaluation of the homogeneous (nonlinear) flapping equation results in highly damped motions for all advance ratios (dotted line). Evaluating the periodic equilibrium solution, we find the stability behavior considerably changed (solid line). The applied forcing function again represents the effect of the blade weight and a linear twist ($\vartheta_1 = -0.2\,\mathrm{rad}$).

As discussed in Ref.[2], the flap stiffness which is required to restrict the steady amplitudes to reasonable values is considerably higher than required for stability. So the deviations in Fig.10 are mainly caused by the high flap amplitudes which, in turn, increase the influence of aerodynamic nonlinearities. At $\mu = 9$, the amplitudes have reached such high values that stall effects are dominating, and the flapping motion becomes unstable.

Flap-Torsional Coupling

A comprehensive description of the coupled flap-torsion motion can be found in Ref.[12]. However, the authors concentrate on high advance ratios due to high forward speed at constant rotor rpm, which is different from the stop-rotor problem investigated here.

Divergence

The first question is, under which conditions the resultant spring effect due to elastic *and* aerodynamic forces tend to be destabilizing. For the coupled linear equations, the static stability boundary is given by

$$\det\left[\operatorname{diag}\underline{\underline{\gamma K}}(\psi) + \underline{\underline{K}}_0\right] = 0 \quad .$$

Solving this equation, we can plot the necessary torsional stiffness over the blade azimuth and advance ratio, see Fig.11. The chosen flap stiffness of $\bar{\omega}_\beta^{nr} = 0.2$ assures static and dynamic stability for the *isolated* flapping degree of freedom.

The left hand diagrams refer to the case in which the feathering axis, the center of gravity and the normal flow aerodynamic center coincide at the 25% chord line. It is seen that only the retreating blade is susceptible to divergence. For the critical blade position at $\psi \approx 240\,\mathrm{deg}$, the necessary torsional stiffness reaches approximately $\bar{\omega}_\vartheta^{nr} = 2.5$ at high advance ratios. If one could optimize the blade with respect to the static stability alone, the necessary stiffness would reduce slightly to $\bar{\omega}_\vartheta^{nr} \approx 2.1$, see Fig.11 right hand side. The high dynamic pressure at the nominal rotor speed (i.e. when the lift always acts at the 25% chord line) prevents the shifting of the feathering axis further towards the 75% line in order to reduce the torsional moments in reverse flow.

It should be noted, however, that for systems with periodic coefficients this static stability is not a necessary condition for dynamic stability.

Dynamic Stability

The following results again refer to the linear equations. Since the coupling effects proved to be relatively small, the flapping stiffness was now set to $\bar{\omega}_\beta^{nr} = 0.1$, which

approximately represents the stability boundary for isolated flapping. The four diagrams of Fig.12 illustrate the dynamic stability of the torsional motion isolated from flapping (left hand side) as well as the coupling effects when f.a. and c.g. are located in a.c.$_1$ (right hand side). The calculated damping values for the torsional motion show the same periodic system characteristics that have been observed for the flapping motion. The regions of parametric resonance (i.e. the regions in which the periodic coefficients have a destabilizing effect), however, move close together due to the high natural frequency in the torsional degree of freedom.

For $\bar{\omega}_\Theta^{nr} = 2.0$ the isolated torsional motion stays stable up to very high advance ratios, while the coupled motions become unstable at approximately $\mu = 10$ (upper diagrams). Yet a slight increase in the torsional stiffness (to $\bar{\omega}_\Theta^{nr} = 2.2$) is sufficient to achieve stability even in the coupled case (upper diagrams).

The stability diagram in Fig.13 gives a further impression of how the torsional degree of freedom influences the blade motion stability. The stability boundaries are found to be dominated by the flapping motion. Only for advance ratios above $\mu = 9$ is the structure of the stability regions obviously affected by the torsional motion. Vice versa, Fig. 14 presents the corresponding stability diagram showing the influence of the torsional stiffness. For isolated torsion the algorithm used here was not able to resolve the close sequence of resonance regions exactly. When the flapping motion is included, the typical structure again arises, while the necessary torsional stiffness is slightly shifted to higher values.

As pointed out previously, the motion may be dynamically stable even if static divergence would occur within a certain azimuth range. This is clearly demonstrated by the examples shown here. Dynamic stability is assured with $\bar{\omega}_\beta^{nr} = 0.1$ and $\bar{\omega}_\Theta^{nr} = 2.0$, (at least up to $\mu = 10$, see Figs.13 and 14), while static stability was found to require values of at least $\bar{\omega}_\beta^{nr} = 0.2$ and $\bar{\omega}_\Theta^{nr} = 2.5$ (for the same μ range, see Fig.11).

Further calculations have been carried out with various locations of the feathering axis and the profile section center of gravity. Two examples are presented in Fig.15. Only marginal improvements were found to be achievable (optimal configuration: f.a. and c.g. at 28% of blade chord). Thus it appears that the classical mass balanced blade design is also a feasible choice for the stop-rotor.

Flap-Lag Coupling

In contrast to flapping and torsion, the isolated lead-lag motion exhibits solely weak parametric resonance. A lead-lag hinge spring stiffness of only $\bar{\omega}_\zeta^{nr} = 0.05$ is sufficient to prevent any parametric destabilization.

For the coupled calculations, a mechanical damper providing 3% critical damping has been modeled in the lag degree of freedom. The presented examples refer to forced solutions due to the aerodynamic and gravity terms $\underline{F}(\psi)$, $\underline{F}_0$ only. As was expected, the coupling effects were relatively small. For nonrotating frequencies of $\bar{\omega}_\beta^{nr} = 0.1$ and $\bar{\omega}_\zeta^{nr} = 1.0$ (i.e. a stiff in-plane rotor), the stability of the flap mode deteriorates slightly, yet all coupled motions stay stable, see Fig. 16. For a soft in-plane rotor ($\bar{\omega}_\beta^{nr} = 0.1$ and $\bar{\omega}_\zeta^{nr} = 0.5$), stronger interaction occurs at advance ratios above $\mu = 5$, and stability is lost at approximately $\mu = 7$, see Fig.17. However, it must be stressed that the flap stiffness was intentionally chosen quite small to provoke any coupling effects. For the values that are required to restrict the flap amplitudes to realistic values, almost no flap-lag interaction was observed.

The calculations presented in Fig.17 were also used to compare the results obtained from linearization and the modified FLOQUET method. The agreement was found to be very good for the least stable modes, while some deviations were noted for the highly damped modes in regions of stronger flap-lag interaction.

Active Control

Because flapping turned out to be the most important degree of freedom, the improvement of its stability and the reduction of its response amplitudes are important objectives in the stop-rotor development. The following straightforward examples show that the application of active control technology may be a possible alternative to the otherwise recommended stiff blade design.

One Possible Concept

As mentioned above, the flapping motion consists of considerable higher-harmonic portions during the start/stop procedure. Moreover, the blades increasingly undergo different external disturbances when rotating at low rotor speed. Hence the individual blade control approach seems to be the appropriate control concept in this case.

Figure 18 shows the signal flow diagram of the linearized flapping equation. The main difficulty arises from the periodic feed-forward gain $\gamma_\beta E_{12}(\psi)$ (see Fig.19, upper left diagram) which complicates the generation of stabilizing flap moments. The relationship between the pitch angle ϑ_{con} and the flap moments even inverts during a certain part of the rotor revolution. As a result of this, a control structure has been chosen that is based on the approximate compensation of this periodic coefficient. Moreover it was investigated, whether it is useful to suppress additionally the periodicity of the spring coefficient $\gamma_\beta K_{11}(\psi)$.

Stability Augmentation

In the first step, an exact E_{12}-compensation was assumed to be realizable. Then, different combinations of feedback loops were modeled to determine how effective they stabilize the flapping motion.

- The compensation of the periodic term of the *damping* coefficient was not found to be efficient, since in most cases even a periodic damping proved to be stabilizing.
- Adding some constant artificial damping through $G_{\beta'}$ improves the stability, however the slope of the real parts with respect to the advance ratio does not change.
- The compensation of the periodic portion of the *spring* coefficient proved to be the most effective means for stability augmentation.
- To feed back the flap angle through G_β corresponds to an additional artificial hinge spring, and is just as efficient as increasing the physical flap stiffness itself.

The effectiveness of the above mentioned G_β-feedback is illustrated by the left hand side of Fig.19. In this example, the unstable flapping motion of an articulated blade ($\bar{\omega}_\beta^{nr}=0$) was successfully stabilized at $\mu=2.5$. It is obvious, however, that the realization of $E_{12}(\psi)$ as part of the control law will impose severe technical difficulties. The calculated time history will hardly match the real one, even if it is determined from a sophisticated mathematical model. Moreover, the zeros of this periodic function temporarily drive the feedback gain to infinity and lead to unreasonably fast pitch control inputs. For this reason the simulations have been repeated with a simple square wave approximation $\hat{E}_{12}(\psi)$ shown on the right side of Fig.19. The stabilizing effect is almost the same, while the control activity drops to practical values.

By defining a fictitious flap stiffness which includes the mechanical stiffness $\bar{\omega}_\beta^{nr}$ and the artificial portion due to the G_β-feedback

$$\bar{\omega}_{fict}^{nr}=\sqrt{\bar{\omega}_\beta^{nr^2}+G_\beta\bar{\Omega}^2}$$

it turned out to be reasonable to increase the feedback gain with the square of the advance ratio. Figure 20 illustrates the stabilizing effect over the advance ratio for $\bar{\omega}_\beta^{nr}=0$. If the optimal E_{12} curve shape is applied, the fictitious stiffness $\bar{\omega}_{fict}^{nr}=0.1$ due to feedback control is directly equivalent to a corresponding mechanical stiffness (left hand diagrams). For the $\hat{E}_{12}$-approximation, the results are slightly worse (middle diagrams), but with $\bar{\omega}_{fict}^{nr}=0.2$, a sufficient damping level is achieved at all advance ratios.

Amplitude Reduction

As pointed out previously, the rotor has been assumed to be unloaded during the start/stop procedure. As soon as the inevitable forcing terms on the right hand side are included, however, the blades exhibit a periodic response and a certain amount of thrust even in pure tangential flow. Hence the rotor must be trimmed through proper control inputs. A possible control structure is illustrated in Fig.21.

The different approaches presented in Fig.22 have been investigated for the present. The mechanical stiffness was set to $\bar{\omega}_\beta^{nr}=0.1$ and only the blade weight term has been considered as forcing function. As shown in the first

row, the uncontrolled rotor increasingly exhibits negative thrust and the flapping motion reaches very high amplitudes $A_n = \sqrt{a_n^2 + b_n^2}$.

The conventional approach would be to apply appropriate collective and cyclic pitch input. The pitch angles necessary to cancel the thrust mean value are moderate, but the decrease of the flap amplitudes is not nearly sufficient (second row of Fig.22). Regarding the shown signal flow diagram, one may assume that the compensation of $E_{12}(\psi)$ through appropriate feed forward control should improve the thrust control. While this principle is to some extent successful with the exact function, the $\hat{E}_{12}(\psi)$-approximation turned out to be less feasible (third row of Fig.22).

The main reason is the non-tangential flow condition caused by the negative coning angle due to the blade weight. So it proved to be a better approach to suppress the collective flap coefficient a_0 even if this generates a small positive thrust. From the fourth row of Fig.22, it is seen that a_0 can be successfully canceled by applying the $\hat{E}_{12}$-approximation. All harmonics A_n of the flapping response decrease considerably, while the remaining thrust does not exceed 3% of the aircraft weight.

The application of feedback control as described in the previous section, however, was found to be most efficient. The amplitudes are considerably reduced, while the thrust remains below 2% even without any additional feed-forward trim control (last row of Fig.22). The effectiveness of this approach becomes more obvious in Fig.23. There, the relative suppression of the maximum flapping angles has been plotted versus the artificial stiffness $\bar{\omega}_{G\beta}^{nr} = \sqrt{G_\beta}\,\bar{\Omega}$. With the approximated $\hat{E}_{12}$ function, a reduction to 3.5% of the open loop value is achievable. At very high feedback gains, however, flap instability can be encountered, caused by a rising amplification of the higher-harmonic components.

Conclusion

This investigation confirmed the importance of the flapping motion for the stop-rotor behavior. The dominating design criterion seems to be the restriction of the flap response amplitudes.

The influence of the torsional motion was not found as strong as expected. With respect to divergence, a torsional stiffness of only $\bar{\omega}_\Theta^{nr} = 2.5$ (with $\bar{\omega}_\beta^{nr} = 0.2$) proved to be sufficient, which follows from the low dynamic pressure at reduced rotor speed. For the dynamic stability, the large lift moment arm in reverse flow turned out to be less critical than the possible inertial coupling due to a displacement of the center of gravity from the feathering axis. It is interesting to note that locating the c.g. in front of the f.e. even destabilizes the coupled flap-lag motion at reduced rotor speeds, while this is a common means to avoid flutter for conventional rotors.

Similarly, the flap-lag coupling proved to be quite weak for the unloaded rotor. Considerable destabilizing interaction only occurred in connection with forced solutions that exhibit unrealistic high flap amplitudes.

In the last chapter, some ideas on the active control of the flapping motion were presented. The investigated examples indicate that even very simple feedback structures can successfully be used to restrict the flap amplitudes and suppress any instability.

The applied mathematical models, however, are based on many simplifying assumptions which have to be examined in detail. It is obvious, for example, that the occurrence of considerable higher-harmonic components in the flapping motion suggests the consideration of at least a few higher-frequency elastic modes.

Appendix

Coupled flap/torsional equation of motion:

$$\underline{\underline{J}}\underline{\chi}'' + \mathrm{diag}\,\underline{\gamma}\,\underline{\underline{D}}(\psi)\underline{\chi}' + \left[\mathrm{diag}\,\underline{\gamma}\,\underline{\underline{K}}(\psi) + \underline{\underline{K}}_0\right]\underline{\chi} = \left[\mathrm{diag}\,\underline{\gamma}\,\underline{\underline{E}}(\psi) + \underline{\underline{E}}_0\right]\underline{\vartheta} + \underline{F}_0$$

$$\underline{\chi} = (\beta, \Theta, \ldots)^T$$

$$\underline{\gamma} = (\gamma_\beta, \gamma_\Theta, \ldots)^T \qquad \underline{\vartheta} = (\vartheta_1, \vartheta_{con}, \vartheta'_{con}, \vartheta''_{con}, \delta)^T$$

Inertial forces:

$$J_{11} = 1 \qquad J_{12} = -\frac{J^{PE}}{J^{PP}} \qquad J_{21} = -\frac{J^{PE}}{J^{EE}} \qquad J_{22} = 1$$

$$\bar{\omega}_\beta^{nr} = \frac{\sqrt{c_\beta / J^{PP}}}{\Omega_{nom}} \qquad \bar{\omega}_\Theta^{nr} = \frac{\sqrt{c_\Theta / J^{SS}}}{\Omega_{nom}}$$

$$K_{0_{11}} = \frac{J^{CP}}{J^{PP}} + \left(\frac{\overline{\omega}_\beta^{nr}}{\overline{\Omega}}\right)^2 \qquad K_{0_{12}} = -\frac{J^{EC}}{J^{PP}}$$

$$K_{0_{21}} = -\frac{J^{EC}}{J^{EE}} \qquad K_{0_{22}} = 1 + \frac{J^{SS}}{J^{EE}}\left(\frac{\overline{\omega}_\Theta^{nr}}{\overline{\Omega}}\right)^2$$

$$E_{0_{11}} = \frac{y_{c.g}}{R}\frac{J^{CC}}{J^{PP}} \qquad E_{0_{12}} = \frac{J^{EC}}{J^{PP}} \qquad E_{0_{14}} = \frac{J^{EP}}{J^{PP}}$$

$$E_{0_{21}} = -\frac{y_{c.g}}{R}\frac{J^{EC}}{J^{EE}} \qquad E_{0_{22}} = -1 \qquad E_{0_{24}} = -1$$

$$F_{0_1} = -\frac{S^P}{J^{PP}}\frac{g}{\Omega^2} \qquad F_{0_2} = \frac{S^E}{J^{EE}}\frac{g}{\Omega^2}$$

$$m_{Bl} = (R-a)\overline{m}$$

$$S^C = \int_m r\,\mathrm{d}m \qquad S^E = \int_m y\,\mathrm{d}m = y_{c.g}m_{Bl}$$

$$S^P = \int_m (r-a)\,\mathrm{d}m$$

$$J^{CC} = \int_m r^2\,\mathrm{d}m \qquad J^{EE} = \int_m y^2\,\mathrm{d}m = J^{SS} + y_{c.g}^2 m_{Bl}$$

$$J^{PP} = \int_m (r-a)^2\,\mathrm{d}m \qquad J^{SS} = \int_m (y-y_{c.g})^2\,\mathrm{d}m$$

$$J^{CP} = \int_m r(r-a)\,\mathrm{d}m$$

$$J^{EC} = \int_m yr\,\mathrm{d}m = y_{c.g}S^C \qquad J^{EP} = \int_m y(r-a)\,\mathrm{d}m = y_{c.g}S^P$$

Lock numbers/2:

$$\gamma_\beta = \frac{\rho C_{l\alpha} l R^4}{2J^{PP}} \qquad \gamma_\Theta = \frac{\rho C_{l\alpha} l^2 R^3}{8J^{EE}}$$

Aerodynamic forces:

$$D_{11}(\psi) = C_4^R - \tfrac{a}{R}C_3^R$$
$$D_{21}(\psi) = -G_3 + \tfrac{a}{R}G_2 + C_2^R\mu\sin\psi$$
$$D_{22}(\psi) = \tfrac{l}{R}(G_2 + 2\overline{D}_2 + \overline{D}_1\mu\sin\psi)\overline{\nu}$$

$$K_{11}(\psi) = C_3^R\mu\cos\psi$$
$$K_{12}(\psi) = -C_4^R - C_3^R\mu\sin\psi$$
$$K_{21}(\psi) = -G_2\mu\cos\psi + \overline{D}_1\mu^2\sin\psi\cos\psi$$
$$K_{22}(\psi) = G_3 - (\overline{D}_2 - G_2)\mu\sin\psi - \overline{D}_1\mu^2\sin^2\psi$$

$$E_{11}(\psi) = C_5^R + C_4^R\mu\sin\psi$$
$$E_{12}(\psi) = C_4^R + C_3^R\mu\sin\psi$$
$$E_{15}(\psi) = C_3^R$$
$$E_{21}(\psi) = -G_4 + (\overline{D}_3 - G_3)\mu\sin\psi + \overline{D}_2\mu^2\sin^2\psi$$
$$E_{22}(\psi) = -G_3 + (\overline{D}_2 - G_2)\mu\sin\psi + \overline{D}_1\mu^2\sin^2\psi$$
$$E_{23}(\psi) = -\tfrac{l}{R}(G_2 + 2\overline{D}_2 + \overline{D}_1\mu\sin\psi)\overline{\nu}$$
$$E_{25}(\psi) = -G_2 + \overline{D}_1\mu\sin\psi$$

$$C_n^R = \overline{D}_n^R - \tfrac{a}{R}\overline{D}_{n-1}^R \qquad G_n = 4\overline{\nu}\overline{D}_n^R - \overline{D}_n$$

$$C_n = \overline{D}_n - \tfrac{a}{R}\overline{D}_{n-1} \qquad \overline{\nu} = \frac{y_{a.c.l}}{l} + \frac{1}{4}$$

$$\overline{D}_n^R(\psi) = \int_A^B x^{n-2}|x + \mu\sin\psi|\,\mathrm{d}x \qquad \overline{D}_n = \int_A^B x^{n-1}\,\mathrm{d}x$$

Coupled flap/lag equation of motion:

$$\underline{\chi}'' + \mathrm{diag}\,\underline{\gamma}\underline{\underline{D}}(\psi)\underline{\chi}' + \left[\mathrm{diag}\,\underline{\gamma}\underline{\underline{K}}(\psi) + \underline{\underline{K}}_0\right]\underline{\chi} + 2\begin{pmatrix} -\beta\zeta' \\ \dots \\ \beta\beta' \end{pmatrix} =$$
$$\mathrm{diag}\,\underline{\gamma}\underline{\underline{E}}(\psi)\underline{\vartheta} + \mathrm{diag}\,\underline{\gamma}\underline{E}(\psi) + \underline{E}_0$$

$$\underline{\chi} = (\beta, \dots, \zeta)^T$$
$$\underline{\gamma} = (\gamma_\beta, \dots, \gamma_\zeta)^T \qquad \underline{\vartheta} = (\vartheta_1, \vartheta_{con}, \dots, \dots, \delta)^T$$

Inertial forces:

$$K_{0_{33}} = \frac{J^{QP}}{J^{PP}} + \left(\frac{\overline{\omega}_\zeta^{nr}}{\overline{\Omega}}\right)^2 \qquad \overline{\omega}_\zeta^{nr} = \frac{\sqrt{c_\zeta / J^{PP}}}{\Omega_{nom}}$$

$$J^{QP} = \int_m a(r-a)\,\mathrm{d}m = aS^P$$

Aerodynamic forces:

$$D_{33}(\psi) = 2(C_4^R - \tfrac{a}{R}C_3^R)$$
$$K_{33}(\psi) = 2C_3^R\mu\cos\psi$$
$$F_3(\psi) = C_4^R + C_3^R\mu\sin\psi$$

Lock number/2:

$$\gamma_\zeta = \frac{\rho C_{d0} l R^4}{2J^{PP}}$$

Matrix elements not mentioned above are equal to zero or have been neglected.

References

[1] E. Kisli, J.V.R. Prasad, Y. Yillikci, Conceptual Design of a Stopped Rotor with Flap Control, 18th European Rotorcraft Forum, Avignon 1992

[2] U. Arnold, Blade Instability of Horizontally Stoppable Rotors, 17th European Rotorcraft Forum, Paper No. 55, Berlin 1991

[3] G. Reichert, U. Arnold, Active Control of Helicopter Ground and Air Resonance, 16th European Rotorcraft Forum, Paper No. III.6.2, Glasgow 1990

[4] M. Kretz, Active Expansion of Helicopter Flight Envelope, 15th European Rotorcraft Forum, Paper No. 53, Amsterdam 1989

[5] N.D. Ham, Helicopter Individual-Blade-Control Research at MIT 1977-1985, Vertica 1/2/1987

[6] B. Panda, I. Chopra, Flap-Lag-Torsion Stability in Forward Flight, Journal of the American Helicopter Society 4/1985

[7] G.R. Neelakantan, G.H. Gaonkar, Feasibility of Simplifying Coupled Lag-Flap-Torsional Models for Rotor Blade Stability in Forward Flight, 10th European Rotorcraft Forum, Paper No. 53, Den Haag 1984

[8] M. Kretz, Stoppable and Stowable Jet-Flap Rotor Concept, 4th European Rotorcraft and Powered Lift Aircraft Forum, Paper No. 46, Stresa, Italy, 1978

[9] M. Kretz, Relaxation of Rotor Limitations by Feedback Control, 33rd Annual Forum of the American Helicopter Society, Washington D.C. 1977

[10] H. Huber, H. Krafka, Studies on Rotor and Flight Dynamics of a Horizontally Stoppable Hingeless Rotor Aircraft, 2nd European Rotorcraft and Powered Lift Aircraft Forum, Paper No. 38, Bückeburg 1976

[11] D.A. Peters, Flap-Lag Stability of Helicopter Rotor Blades in Forward Flight, Journal of the American Helicopter Society 4/1975

[12] G.J. Sissingh, W.A. Kuczynski, Investigations on the Effect of Blade Torsion on the Dynamics of the Flapping Motion, Journal of the American Helicopter Society 2/1970

[13] H. Krafka, Sobetzko, Aerodynamische Untersuchungen der Transition eines VSTOL-Flugzeuges mit Faltrotoren anhand von Windkanalmessungen, 1. und 2. Teilbericht, MBB München, Juli 1970

[14] R.P. White, Instabilities Associated with a Rotor Blade Stopped in Flight, Journal of the American Helicopter Society 2/1969

[15] G.J. Sissingh, Dynamics of Rotors Operating at High Advance Ratios, Journal of the American Helicopter Society 3/1968

[16] R.W. Prouty, R.E. Donham, Aerodynamic Considerations of Stopping a Rotor in Flight, American Helicopter Society, 23rd Annual National Forum Proceedings, Washington D.C. 1967

[17] R.E. Donham, W.P. Harvick, Analysis of Stowed Rotor Aeroelastic Characteristics, Journal of the American Helicopter Society 1/1967

[18] G. Reichert, B. Mühlig-Versen, Steuerungs- und Regelungsprobleme bei Drehflüglern mit entlasteten Rotoren, Bericht DF 40, Bölkow GmbH, Ottobrunn 1966

[19] P.W. Theriault, I.H. Culver, L.Celniker, Considerations Relative to Stopping a Rotor in Forward Flight, American Helicopter Society, 21st Annual National Forum Proceedings, Washington D.C. 1965

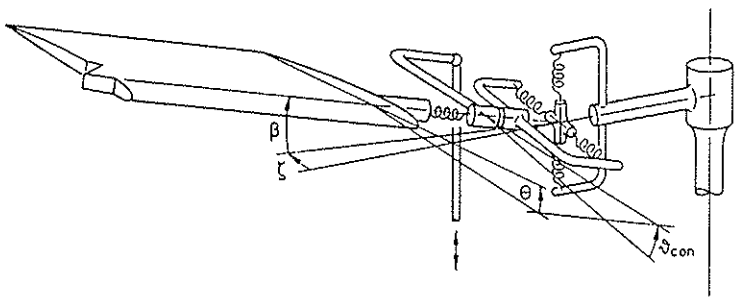

Figure 1: Rotor blade model

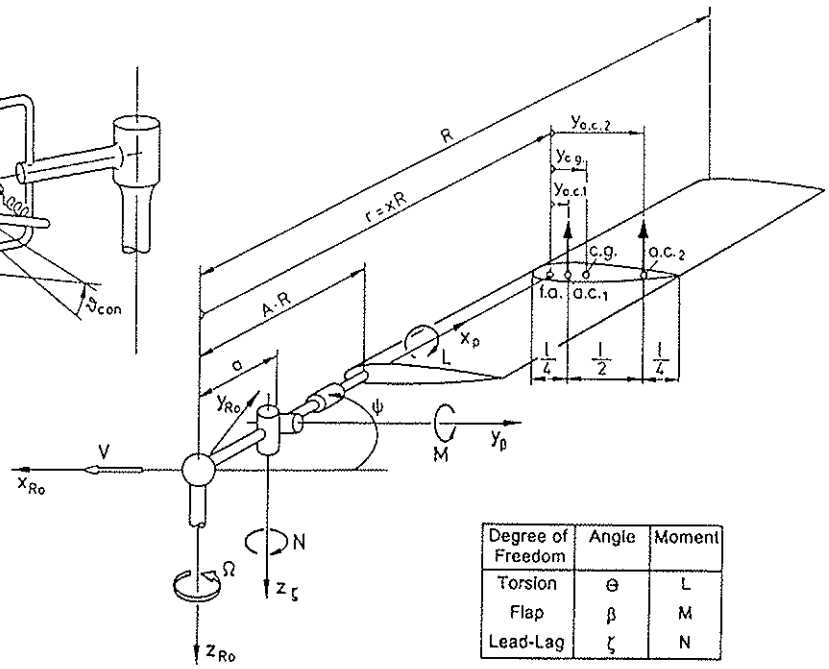

Degree of Freedom	Angle	Moment
Torsion	θ	L
Flap	β	M
Lead-Lag	ζ	N

Figure 2: Definition of blade geometry

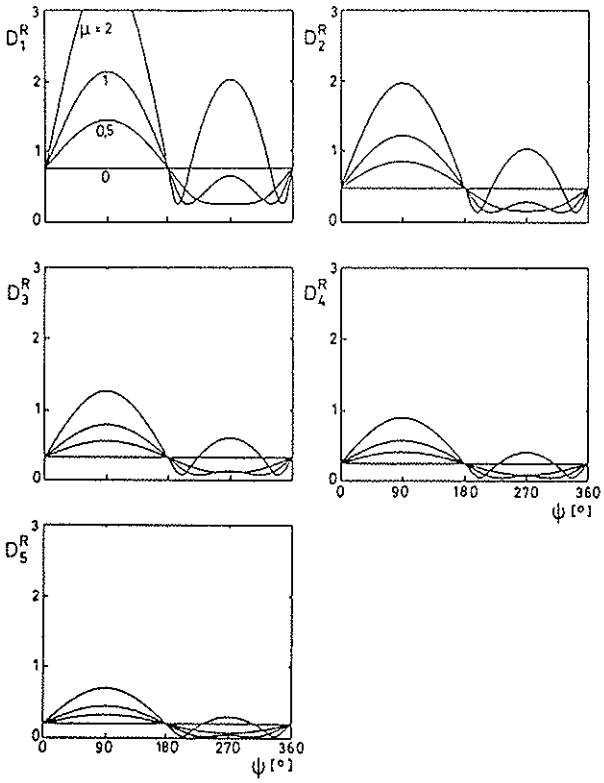

Figure 3: *Periodic blade integrals considering reverse flow*

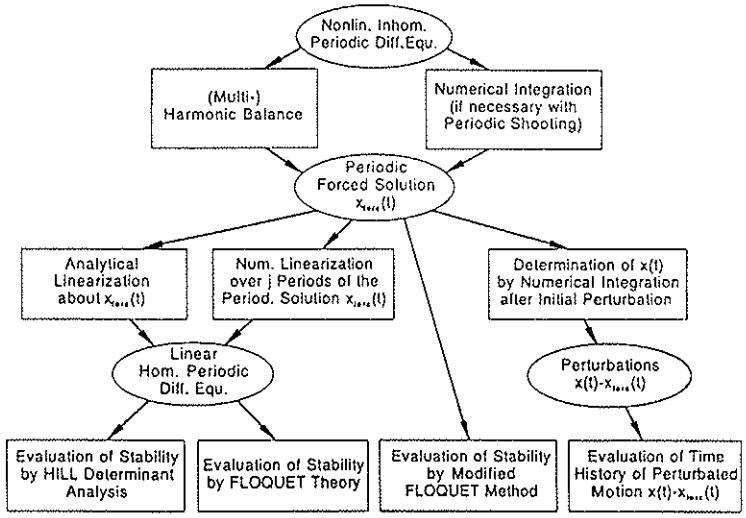

Figure 4: *Different procedures to determine the stability of periodic non-linear equations of motion*

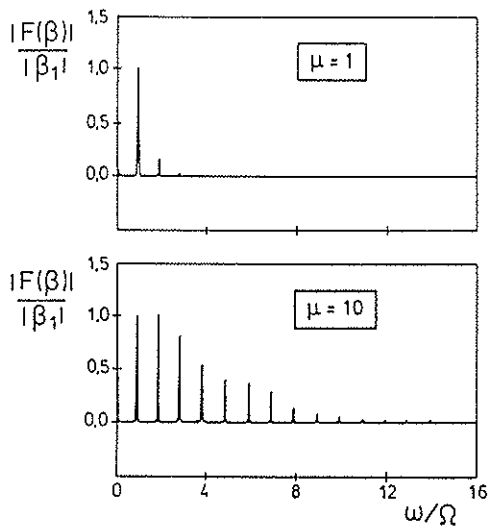

Figure 5: *Fourier Transform of the steady flapping motion* ($\varpi_\beta^{nr} = 0.17$), *forcing function: blade weight,* $\vartheta_1 = -0.2$, $\vartheta_0 = 9.2°$, $\vartheta_c = \vartheta_s = 1°$

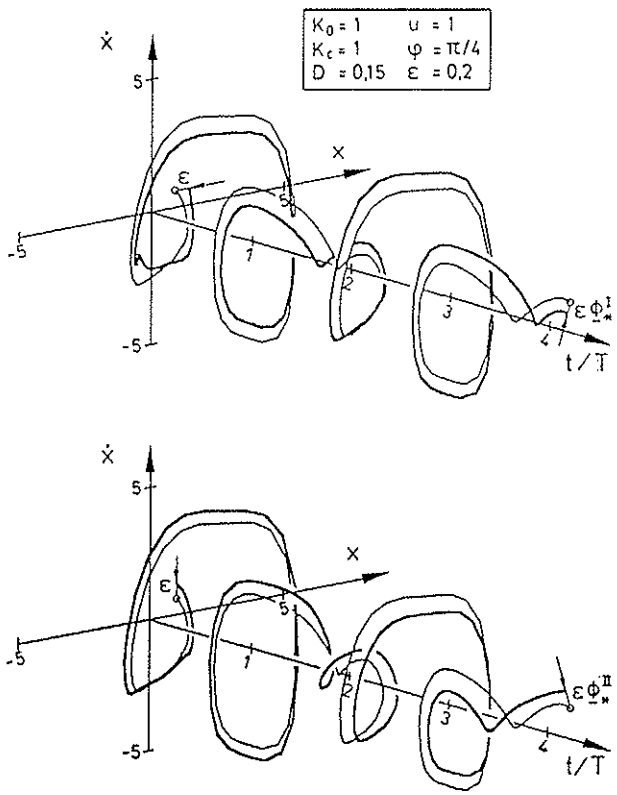

Figure 6: *Determination of Floquet transition matrix by perturbing the periodic forced solution*

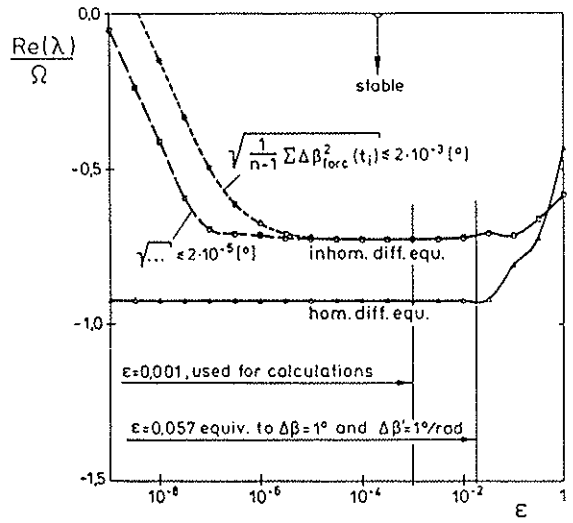

Figure 7: Flapping stability computed by modified FLOQUET method ($\bar{\omega}_\beta^{nr} = 0.12$, $\mu = 5$), forcing function: blade weight, $\vartheta_1 = -0.2$, $\vartheta_0 = 9.2°$

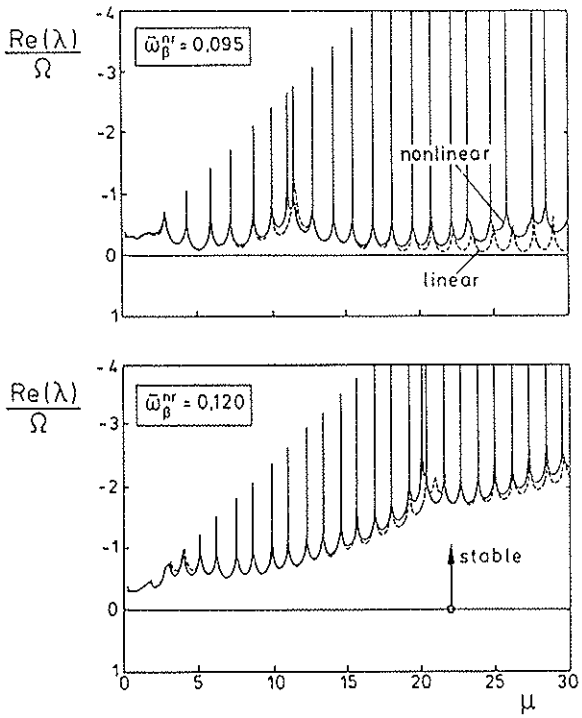

Figure 8: Flapping stability, comparison of results from linear and nonlinear homogeneous equation

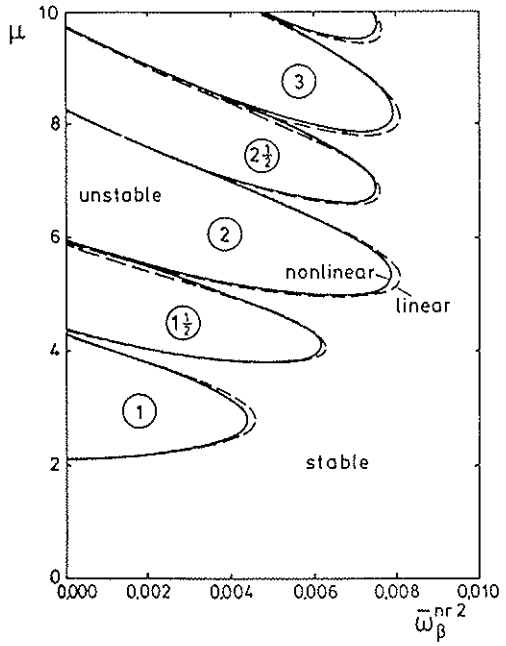

Figure 9: Flapping stability diagram, comparison of results from linear and nonlinear homogeneous equation

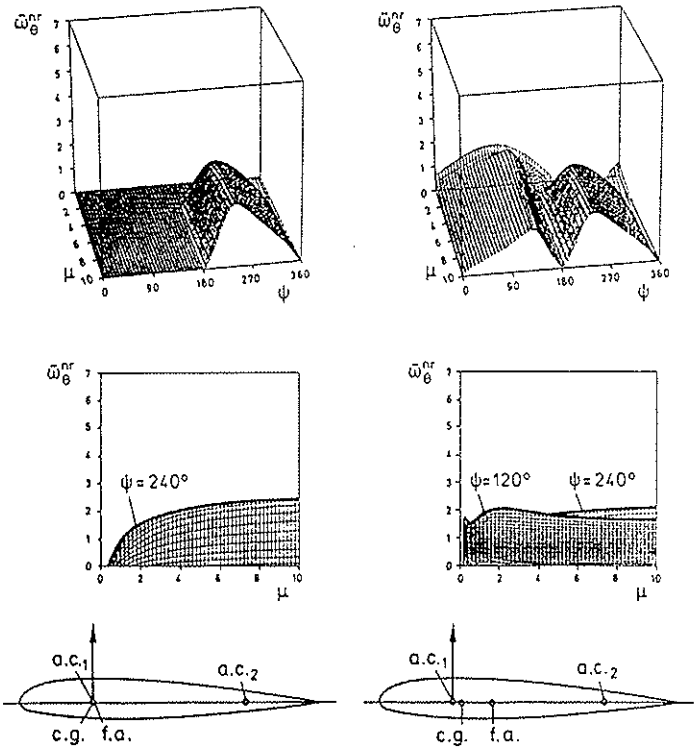

Figure 11: Flap-torsion divergence ($\bar{\omega}_\beta^{nr} = 0.2$)

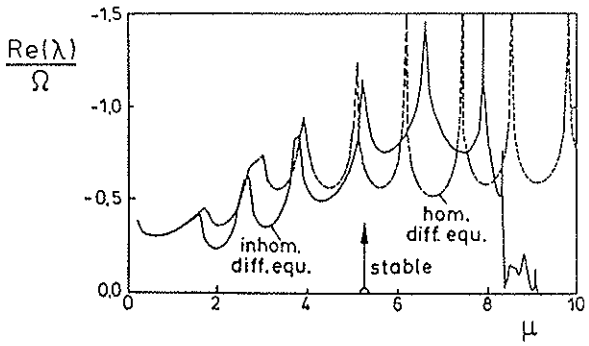

Figure 10: Flapping stability ($\bar{\omega}_\beta^{nr} = 0.12$), effect of forcing function: blade weight, $\vartheta_1 = -0.2$, $\vartheta_0 = 9.2°$

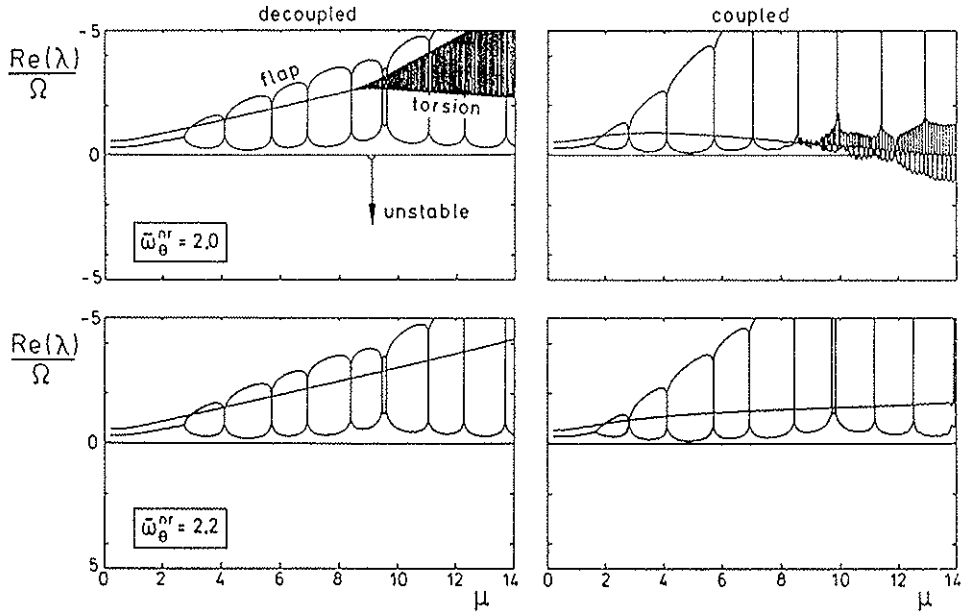

Figure 12: Flap-torsion stability ($\bar{\omega}_\beta^{nr} = 0.1$, $y_{c.g.} = y_{a.c._1} = 0$)

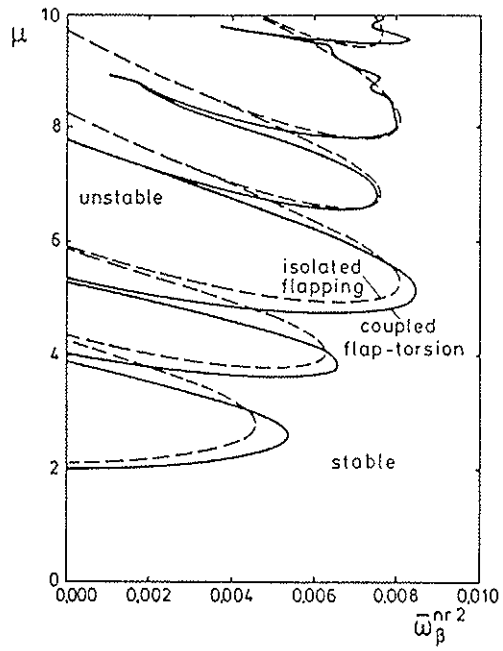

Figure 13: Flap-torsion stability diagram ($\bar{\omega}_\Theta^{nr} = 2.0$, $y_{c.g.} = y_{a.c._1} = 0$)

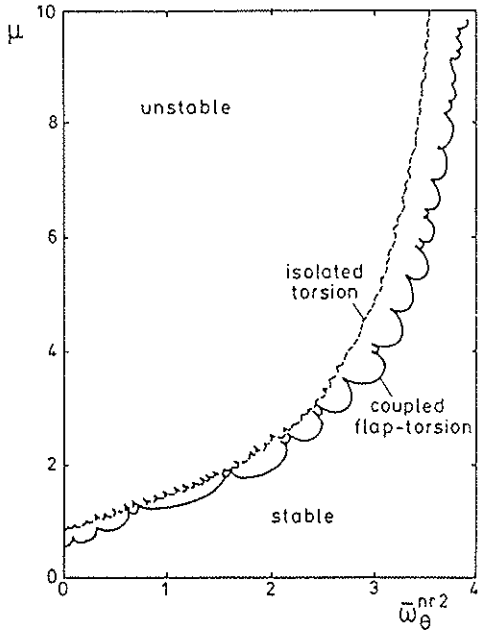

Figure 14: Flap-torsion stability diagram ($\bar{\omega}_\beta^{nr} = 0.1$, $y_{c.g.} = y_{a.c._1} = 0$)

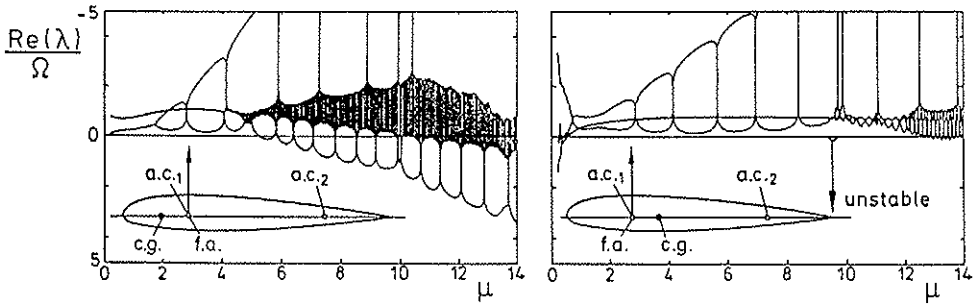

Figure 15: Effect of c.g. and f.a. location on flap-torsion stability ($\bar{\omega}_\beta^{nr} = 0.1$, $\bar{\omega}_\Theta^{nr} = 2.0$)

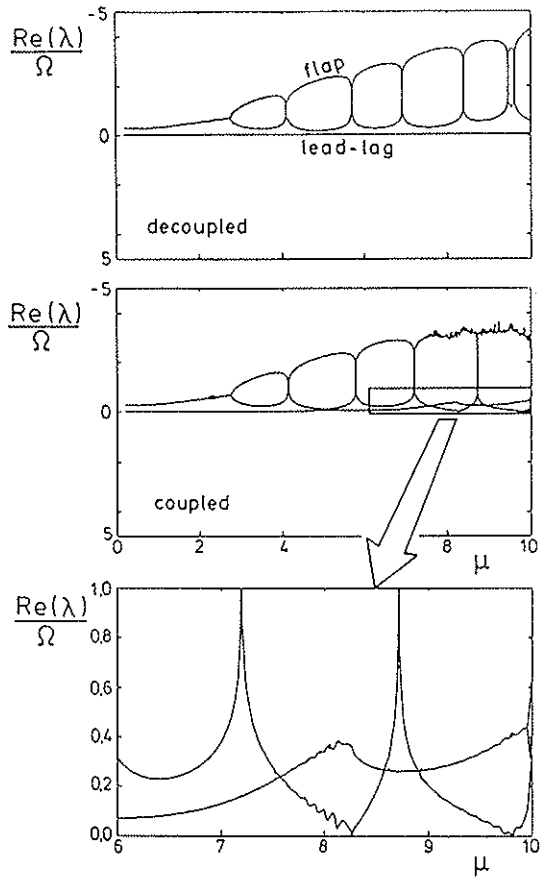

Figure 16: Flap-lag stability ($\bar{\omega}_\beta^{nr} = 0.1, \bar{\omega}_\zeta^{nr} = 1.0$)

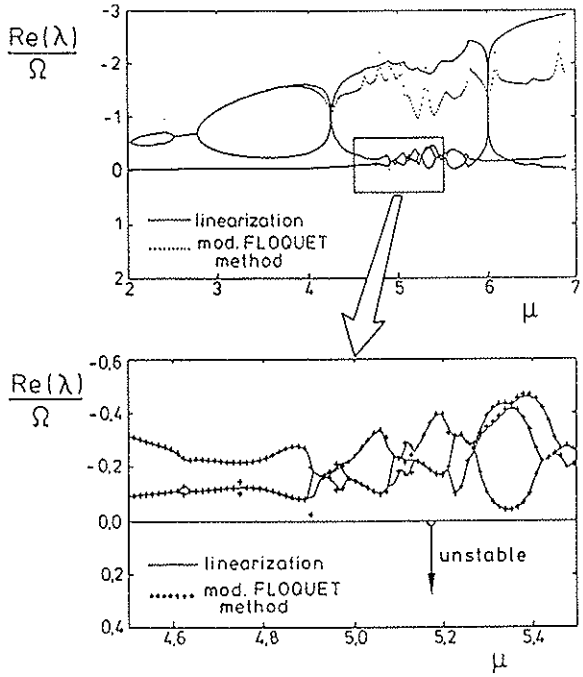

Figure 17: Flap-lag stability ($\bar{\omega}_\beta^{nr} = 0.1, \bar{\omega}_\beta^{nr} = 0.5$), comparison of results from linearization and modified FLOQUET method

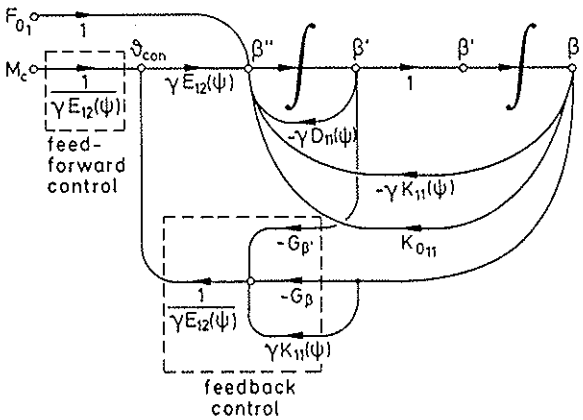

Figure 18: Signal flow diagram of controlled flap dynamics

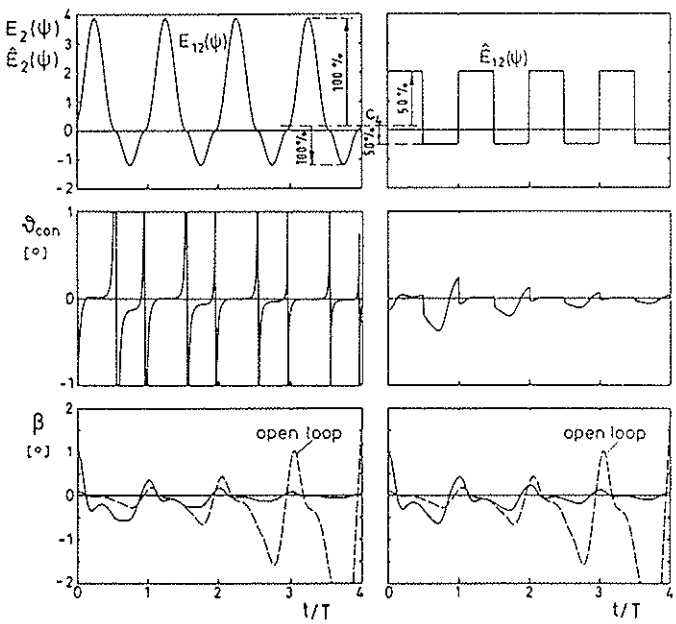

Figure 19: Stabilization of flap motion by artificial stiffness ($\mu = 2.5, \bar{\omega}_\beta^{nr} = 0, G_\beta = 1$, $\bar{\omega}_{\beta_{fict}}^{nr} = 0.08$), comparison of exact ($E_{12}$) and approx. ($\hat{E}_{12}$) feed forward function

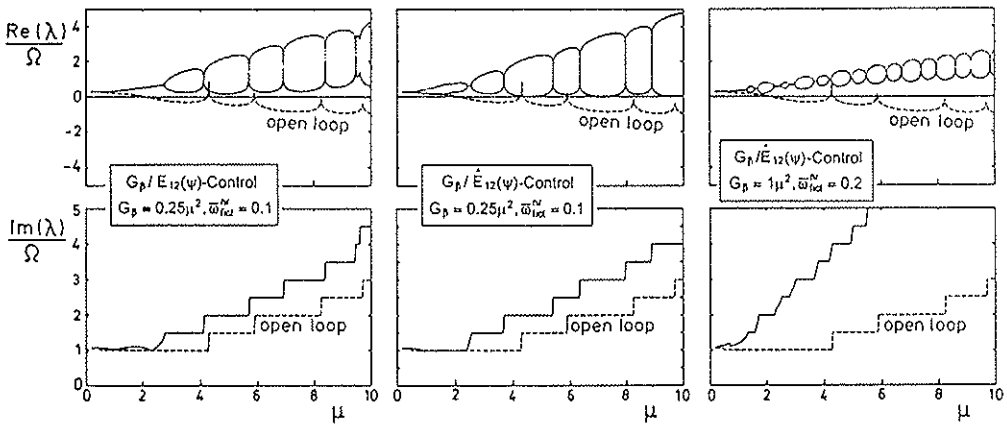

Figure 20: Stabilization of flap motion by artificial stiffness, effect of $E_{12}(\psi)$-approximation and feedback gain G_β

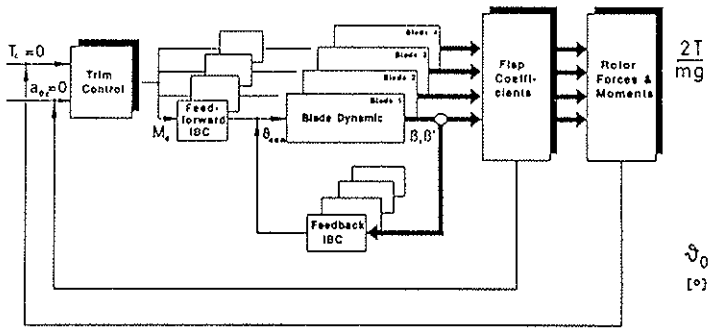

Figure 21: Principle of control structure for rotor trim and flap amplitude reduction

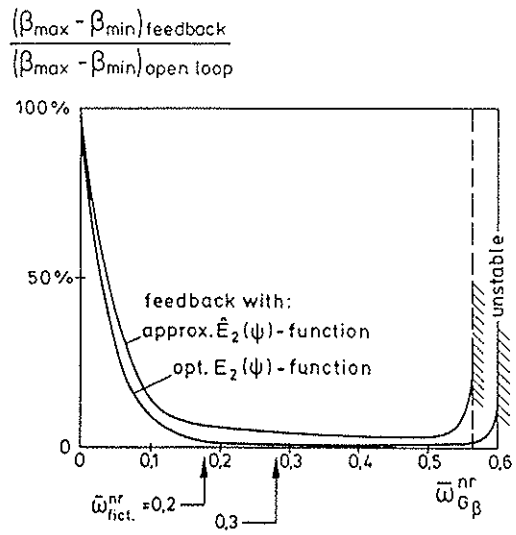

Figure 23: Effect of feedback gain on flap amplitude suppression ($\mu = 5, \bar{\omega}_\beta^{nr} = 0.1$), forcing function: blade weight only

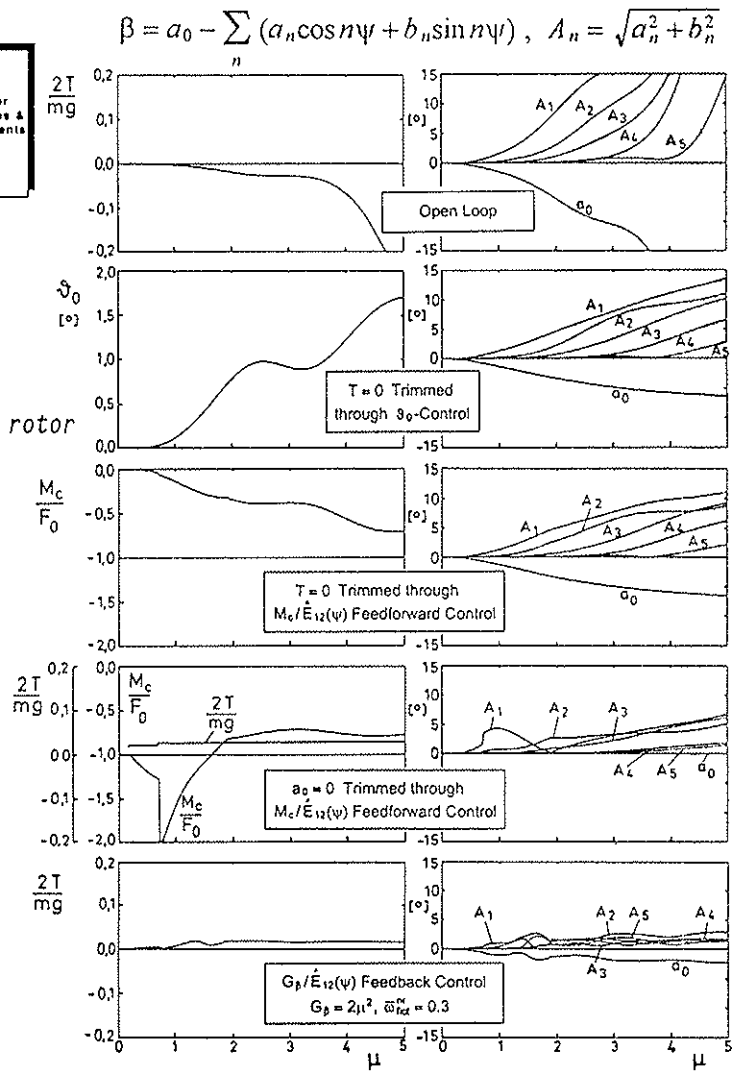

Figure 22: Different methods of rotor trim and flap amplitude reduction ($\bar{\omega}_\beta^{nr} = 0.1$), forcing function: blade weight only